Euclid near infrared spectrometer and photometer instrument NISP in space

William Gillard, Stefano Dusini, Knud Jahnke, Eric Prieto, Natalia Auricchio, Remi Barbier, Evandro Balbi, Andrea Balestra, Paola Battaglia, Vito Capobianco, et al.

Euclid Near Infrared Spectrometer and Photometer instrument NISP in space

On behalf of the Euclid Collaboration: W. Gillard[*1], S. Dusini[2], K. Jahnke[3], E. Prieto[4], N. Auricchio[5], R. Barbier[6], E. Balbi[7], A. Balestra[8], P. Battaglia[5], V. Capobianco[9], R. Chary[10,11], L. Corcione[9], F. Cogato[12,5], G. Delucchi[13,7], S. Ferriol[6], E. Franceschi[5], L. Gabarra[14], F. Gianotti[5], F. Grupp[15,16], E. Lentini[17], S. Ligori[9], E. Medinaceli[5], G. Morgante[5], K. Paterson[3], E. Romelli[18], L. Sauniere[1], M. Schirmer[3], C. Sirignano[19,2], G. Testera[7], M. Trifoglio[5], A. Troja[19,2], L. Valenziano[5,20], Y. Copin[6], M. Frailis[18], B. Kubik[6], M. Scodeggio[21], J.-C. Barriere[22], M. Berthe[23], C. Bodendorf[15], A. Caillat[4], M. Carle[4], R. Casas[24,25], H. Cho[26], A. Costille[4], F. Ducret[4], B. Garilli[21], W. Holmes[26], F. Hormuth[27], A. Hornstrup[28,29], M. Jhabvala[30], R. Kohley[31], D. Le Mignant[4], P. B. Lilje[32], I. Lloro[33], C. Padilla[34], G. Polenta[35], J.-C. Salvignol[36], G. Seidel[3], B. Serra[37], A. Secroun[1], G. Smadja[6], L. Stanco[2], R. Toledo-Moreo[38], S. Anselmi[2,19,39], E. Borsato[19,2], L. Caillat[1], C. Colodro-Conde[40], V. Conforti[5], J. E. Davies[3], A. Renzi[19,2], F. Dal Corso[2], S. Davini[7], A. Derosa[5], J. J. Diaz[41], S. Di Domizio[13,7], D. Di Ferdinando[42], R. Farinelli[5], A. G. Ferrari[43,42], F. Fornari[20], F. Giacomini[42], O. Krause[3], F. Laudisio[2], J. Macias-Perez[44], J. Marpaud[44], N. Mauri[43,42], R. da Silva[45,35], M. Niclas[1], F. Passalacqua[19,2], I. Risso[17], P. Lagier[1], A. N. Sorensen[46], P. Stassi[44], J. Steinwagner[15], M. Tenti[42], C. Thizy[47], S. Tosi[13,7], R. Travaglini[42], O. Tubio[40], C. Valieri[42], S. Ventura[2], C. Vescovi[44], and J. Zoubian[1]

[1]Aix-Marseille Université, CNRS/IN2P3, CPPM, Marseille, France
[2]INFN-Padova, Via Marzolo 8, 35131 Padova, Italy
[3]Max-Planck-Institut für Astronomie, Königstuhl 17, 69117 Heidelberg, Germany
[4]Aix-Marseille Université, CNRS, CNES, LAM, Marseille, France
[5]INAF-Osservatorio di Astrofisica e Scienza dello Spazio di Bologna, Via Piero Gobetti 93/3, 40129 Bologna, Italy
[6]Université Claude Bernard Lyon 1, CNRS/IN2P3, IP2I Lyon, UMR 5822, Villeurbanne, F-69100, France
[7]INFN-Sezione di Genova, Via Dodecaneso 33, 16146, Genova, Italy
[8]INAF-Osservatorio Astronomico di Padova, Via dell'Osservatorio 5, 35122 Padova, Italy
[9]INAF-Osservatorio Astrofisico di Torino, Via Osservatorio 20, 10025 Pino Torinese (TO), Italy
[10]Infrared Processing and Analysis Center, California Institute of Technology, Pasadena, CA 91125, USA
[11]University of California, Los Angeles, CA 90095-1562, USA
[12]Dipartimento di Fisica e Astronomia "Augusto Righi" - Alma Mater Studiorum Università di Bologna, via Piero Gobetti 93/2, 40129 Bologna, Italy
[13]Dipartimento di Fisica, Università di Genova, Via Dodecaneso 33, 16146, Genova, Italy
[14]Department of Physics, Oxford University, Keble Road, Oxford OX1 3RH, UK
[15]Max Planck Institute for Extraterrestrial Physics, Giessenbachstr. 1, 85748 Garching, Germany
[16]Universitäts-Sternwarte München, Fakultät für Physik, Ludwig-Maximilians-Universität München, Scheinerstrasse 1, 81679 München, Germany
[17]Dipartimento di Fisica, Università degli studi di Genova, and INFN-Sezione di Genova, via Dodecaneso 33, 16146, Genova, Italy
[18]INAF-Osservatorio Astronomico di Trieste, Via G. B. Tiepolo 11, 34143 Trieste, Italy
[19]Dipartimento di Fisica e Astronomia "G. Galilei", Università di Padova, Via Marzolo 8, 35131 Padova, Italy
[20]INFN-Bologna, Via Irnerio 46, 40126 Bologna, Italy
[21]INAF-IASF Milano, Via Alfonso Corti 12, 20133 Milano, Italy
[22]CEA-Saclay, DRF/IRFU, departement d'ingenierie des systemes, bat472, 91191 Gif sur Yvette cedex, France
[23]Université Paris-Saclay, Université Paris Cité, CEA, CNRS, AIM, 91191, Gif-sur-Yvette, France
[24]Institut d'Estudis Espacials de Catalunya (IEEC), Edifici RDIT, Campus UPC, 08860 Castelldefels, Barcelona, Spain
[25]Institute of Space Sciences (ICE, CSIC), Campus UAB, Carrer de Can Magrans, s/n, 08193 Barcelona, Spain

[26]Jet Propulsion Laboratory, California Institute of Technology, 4800 Oak Grove Drive, Pasadena, CA, 91109, USA
[27]Felix Hormuth Engineering, Goethestr. 17, 69181 Leimen, Germany
[28]Technical University of Denmark, Elektrovej 327, 2800 Kgs. Lyngby, Denmark
[29]Cosmic Dawn Center (DAWN), Denmark
[30]NASA Goddard Space Flight Center, Greenbelt, MD 20771, USA
[31]ESAC/ESA, Camino Bajo del Castillo, s/n., Urb. Villafranca del Castillo, 28692 Villanueva de la Cañada, Madrid, Spain
[32]Institute of Theoretical Astrophysics, University of Oslo, P.O. Box 1029 Blindern, 0315 Oslo, Norway
[33]NOVA optical infrared instrumentation group at ASTRON, Oude Hoogeveensedijk 4, 7991PD, Dwingeloo, The Netherlands
[34]Institut de Física d'Altes Energies (IFAE), The Barcelona Institute of Science and Technology, Campus UAB, 08193 Bellaterra (Barcelona), Spain
[35]Space Science Data Center, Italian Space Agency, via del Politecnico snc, 00133 Roma, Italy
[36]European Space Agency/ESTEC, Keplerlaan 1, 2201 AZ Noordwijk, The Netherlands
[37]European Southern Observatory, Karl-Schwarzschild Str. 2, 85748 Garching, Germany
[38]Universidad Politécnica de Cartagena, Departamento de Electrónica y Tecnología de Computadoras, Plaza del Hospital 1, 30202 Cartagena, Spain
[39]Laboratoire Univers et Théorie, Observatoire de Paris, Université PSL, Université Paris Cité, CNRS, 92190 Meudon, France
[40]Instituto de Astrofísica de Canarias, Calle Vía Láctea s/n, 38204, San Cristóbal de La Laguna, Tenerife, Spain
[41]Instituto de Astrofísica de Canarias (IAC); Departamento de Astrofísica, Universidad de La Laguna (ULL), 38200, La Laguna, Tenerife, Spain
[42]INFN-Sezione di Bologna, Viale Berti Pichat 6/2, 40127 Bologna, Italy
[43]Dipartimento di Fisica e Astronomia "Augusto Righi" - Alma Mater Studiorum Università di Bologna, Viale Berti Pichat 6/2, 40127 Bologna, Italy
[44]Univ. Grenoble Alpes, CNRS, Grenoble INP, LPSC-IN2P3, 53, Avenue des Martyrs, 38000, Grenoble, France
[45]INAF-Osservatorio Astronomico di Roma, Via Frascati 33, 00078 Monteporzio Catone, Italy
[46]Niels Bohr Institute, University of Copenhagen, Jagtvej 128, 2200 Copenhagen, Denmark
[47]Centre Spatial de Liege, Universite de Liege, Avenue du Pre Aily, 4031 Angleur, Belgium

ABSTRACT

Launched successfully on July 1st, 2023, *Euclid*, the M2 mission of the ESA cosmic vision program, aims mainly at understanding the origin of the accelerated expansion of the Universe. Along with a visible imager VIS, it is equipped with the NISP instrument, a Near Infrared Spectrometer and Photometer, bespoke tailored to perform a 3D mapping of the observable Universe. It operates in the near-infrared spectral range, from 900 nm to 2000 nm with 2 observing modes: as a spectrometer, the NISP instrument will permit measuring millions of galaxy spectroscopic redshifts over the 6.5 years lifetime of the *Euclid* mission; as a photometer, it will obtain photometric redshifts of billions of galaxies. This paper provides a description of the NISP instrument, its scientific objectives, and offers an assessment of its current performance in flight.

Keywords: Infrared, Space Instrument, Cosmology survey, slitless spectroscopy, photometry, *Euclid*, NISP, operational Mission

1. INTRODUCTION

The *Euclid* mission [1] is a cosmological survey mission in the European Space Agency (ESA)'s cosmic vision program that has been formally adopted in June 2012 by the ESA's Science Program Committee. The *Euclid* mission, which encompasses the satellite, the survey strategy and its processing pipeline, is designed to investigate the origin of the accelerated expansion of the Universe as well as the nature of dark Energy and dark matter, which together contribute to about 95 % of the universe's total mass-energy content and play a fundamental role in shaping the universe's large-scale structures and its evolution over time. To do so, *Euclid* is probing the

* gillard@cppm.in2p3.fr

Universe through two main techniques: one is the study of galaxy clustering through redshift measurements of approximately 25 million galaxies across $0.9 < z < 1.8$; the second is the study of weak gravitational lensing, with the evaluation of subtle distortions in the shapes of approximately 1.5 billion galaxies induced by dark matter structures disseminated along the line of sight.

The *Euclid* spacecraft is equipped with two state-of-the-art instruments: the VIS [2], which is a visible camera with an angular resolution of $0\farcs1$ pixel^{-1} that provides images of high optical quality allowing galaxies' shear measurements; the NISP [3], which is a Near-Infrared Spectrometer and Photometer dedicated to the redshift measurements of tens of thousands of objects per exposed field. Both instruments share the same field of view (FoV) of $0.54\,\mathrm{deg}^2$.

The *Euclid* spacecraft with its instruments, following over a decade of meticulous development, was successfully launched on the 1st of July 2023 from Cape-Canaveral atop a Falcon-9 rocket provided by SpaceX. By the end of July 2023, the *Euclid* spacecraft reached its operational position orbiting the second Lagrange Point (L2) along a Lissajous orbit. After about 6 months of commissioning, calibration, and performance verification, *Euclid* started its cosmological survey in February 2024.

This paper aims to summarise the status of the Near-Infrared Spectrometer and Photometer (NISP) instrument in flight. It starts with a brief description of the NISP instrument before detailing its status and it's in-flight performance.

2. OVERVIEW OF THE NISP INSTRUMENT

The NISP instrument has been designed to provide the redshift measurements needed for galaxy clustering and weak lensing analyses. It encompasses the functions of a photometer and of a spectrometer. As a photometer, the NISP instrument captures photometric images in three near-infrared bandpasses spanning from 900 to 2000 nm. Those images complement ground observations and VIS images for the photometric redshift determination of galaxies. As a spectrometer, the NISP instrument achieves slit-less spectroscopy to provide redshift measurements between 0.9 to 1.8 with a precision of the order of $\sigma_z = 0.001(1+z)$. This precision is needed for conducting detailed galaxy clustering analyses from which the dark matter contribution and equation of state of dark energy will be assessed at percent level accuracy.

Figure 1 presents the NISP instrument. It comprises a mechanical structure [Mechanical Support Structure (NI-SA-ST)] that supports and holds in place the near-infrared focal plane (NI-DS) and the optical system (NI-OA). The NISP mechanical structure is made of silicon carbide (SiC) to ensure it can withstand launch vibrations and maintain thermal stability below $\pm 0.3\,\mathrm{K}$, thus keeping NISP's optics aligned with the focal plane over the 6 years of flight operations [4]. The heat transfer between the payload module and the instrument is minimized to $\simeq 0.035\,\mathrm{W\,K^{-1}}$, thanks to Invar hexapod (NI-SA-HP) that allows the NISP instrument to operate at temperature below 140 K.

The NISP optics is composed of four meniscus lenses with diameters of 130 cm to 160 cm, assembled in the camera lenses (CaLA) and the corrector lens (CoLA). This reduces the telescope's $F/20.4$ focal ratio to $F/10.4$ enabling a compact instrument design. Between the CoLA and CaLA lenses, a filter wheel (NI-FWA) and a grism wheel (NI-GWA) allow the selection of filters or grisms for photometric or slit-less exposure, respectively. The filter wheel houses a set of three filters [5], namely Y_{E} (950–1212 nm), J_{E} (1168–1567 nm), and H_{E} (1522–2021 nm), as well as an 'open' and a 'closed' position to acquire dark frames. The grism wheel contains a set of three 'red' grisms (1206–1892 nm) dispersing light in either 0°, 180° or 270° on the focal plane, as well as a single 'blue' grism (926–1366 nm) with dispersion direction of 0° and an 'open' position.

During ground test campaign on NISP flight model, a non conformity was identified on the grism that disperses light at 270°, leading to poor image quality. After assessing the risk associated with dismantling the instrument or changing *Euclid* survey strategy, it was determined that the most feasible solution was to proceed with flight hardware as is. The observation strategy evolved to replace exposures taken with non-conforming grism with exposures using alternative grisms, tilted by ±4° as will be shown later in Figure 3.

The camera lens (CaLA) focalises the light onto the focal plane array (NI-DS), composed of 4 × 4 near-infrared HgCdTe detectors of 2k × 2k pixels with 2.3 µm cut-off, which were manufactured by Teledyne Imaging

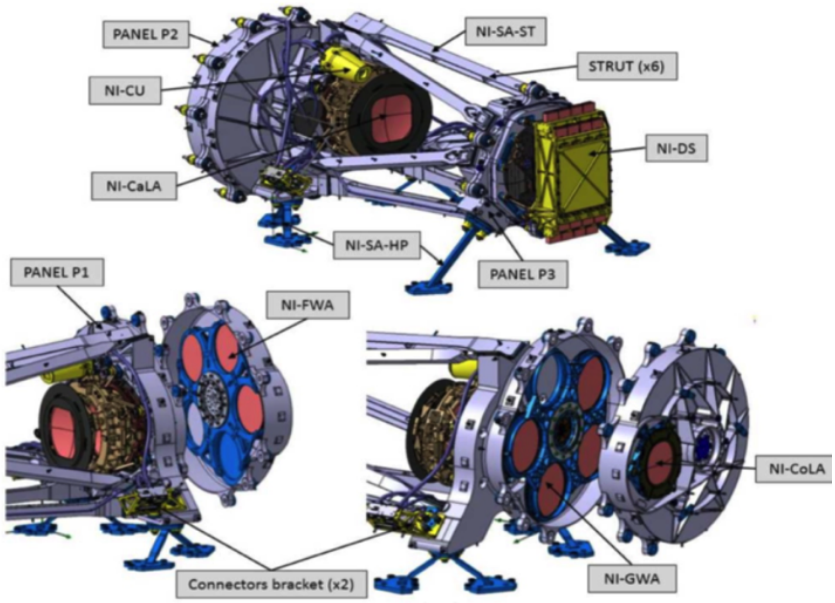

Figure 1: Expanded view of the NISP instrument [6].

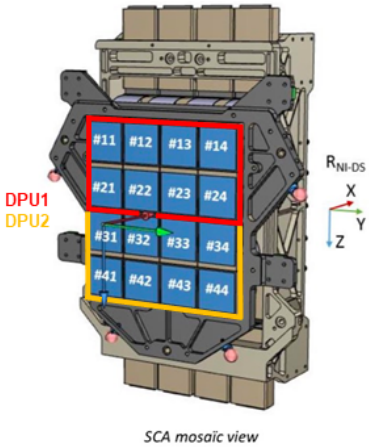

Figure 2: Front view on the NISP focal plane array. Detectors (blue squares) are identified with a 2 digit number that gives their location onto the detector mosaic. Yellow and red boxes highlight which detectors are controlled by which DPU.

Sensors for the *Euclid* mission. These detectors are passively cooled to an operational temperature of the order of 95 K with a stability better than ±4 mK over the duration of a nominal dither which last for about 1210 second.

With a pixel size of 18 µm and $F/10.4$ focal ratio, the NISP has a spatial sampling of $0\farcs3\,\mathrm{pixel}^{-1}$. A calibration unit (NI-CU) containing two sets of five LEDs[†] emitting at five wavelengths covering the NISP bandpass, provides a homogeneous illumination flat, with less than 0.1 % variation over 100 pixels, for calibration of the small-scale pixel response and detector linearity.

The commanding and control of the instrument is achieved by the NISP warm electronics located in the warm environment of the service module of the spacecraft. The NISP instrument operations, including the rotation of the filter and grism wheels as well as calibration unit, are driven by the Instrument Control Unit (ICU) and its on-board application software. The ICU also acts as the main interface with the satellite, receiving telecommands (TC) and sending housekeeping telemetry (TM) to the spacecraft. It also interfaces with two Data Processing Unit (DPU), also part of the NISP's warm electronics, that synchronously command half of the NISP focal-plane's detectors, as shown on Figure 2.

The NISP's detectors acquire signal in a so-called Multiple Accumulated (MACC) mode : Charge generated in pixel by incoming photon accumulate and are non-destructively sampled during the integration time at a constant frame cadence of 1.45408 s; Some of the frames may be dropped[‡] while the integration of the incoming photons continues. At the end of the exposure, the signal per pixel is composed of n_g groups of n_f consecutive read frames separated by n_d dropped frames. This method allows the statistical treatment of the consecutive frames.

Data coming from each detector's front-end electronics (SIDECAR asics) flow to the corresponding Detector Control Unit (DCU) that average a predefined number of read frames per groups; then, the resulting co-added frame are transferred to the DPU, which evaluates the accumulated charge based on a linear fit of the integrated signal per groups over the exposure time [7].

The NISP then transmits to the Mass Memory Unit (MMU) of the spacecraft a compressed file with the slope of the fits, which provides an estimate of the incoming photon flux, together with a quality factor of the

[†]one set for nominal operation plus one redundant set.

[‡]not readout

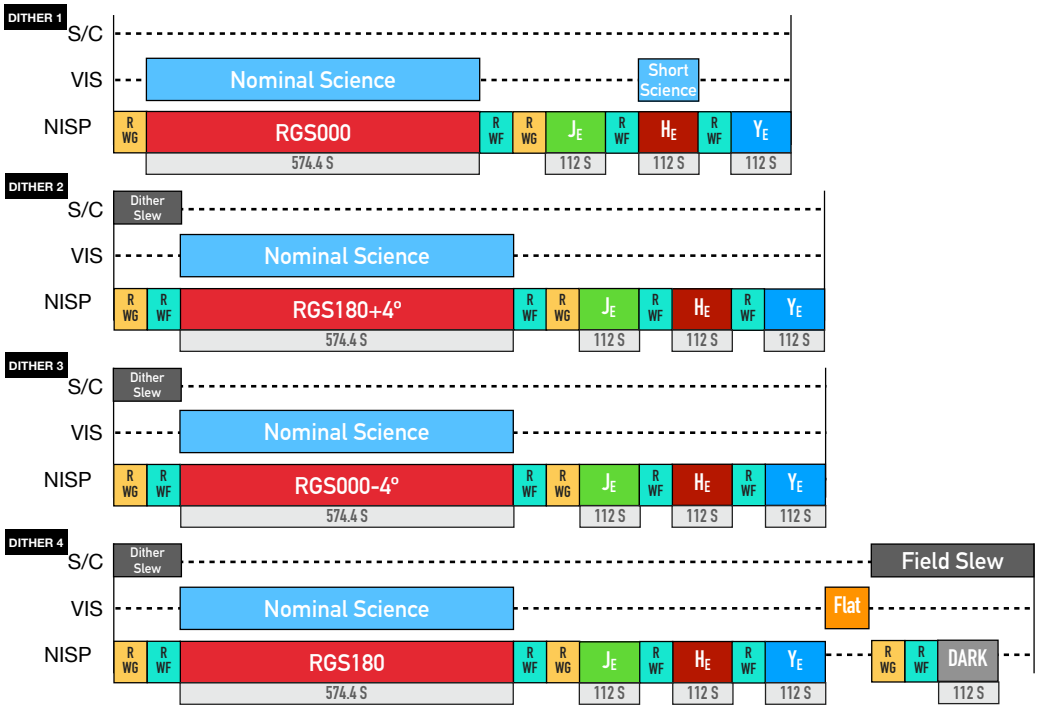

Figure 3: Illustration of the NISP observation sequence.

linear fits. At this point, it is important to note that the processing of the data performed by the DPU can be done in parallel to the following exposure as long as subsequent exposure time is longer than DPU processing time of the previous exposure.

Figure 3 illustrates the reference observation sequence of the NISP instrument. The sequence consists of four *dithers*, each composed by a spectroscopic exposure of about 574.4 s of exposure time[§], which correspond to an integration time[¶] of 549.6 s, acquired in parallel to a VIS exposure, followed by three photometric exposures of 112 s of exposure times each, which corresponds to an integration time of 87.2 s. In between each exposure, filter and grism wheel are rotated to arrange the requested filter or grism in front of the entrance pupil of the instrument. During this sequence, the NISP instrument acquires data in two modes:

- The spectroscopic mode: during spectroscopic exposure in nominal operation, 15 groups, each made of 16 read frames, are averaged together; between groups, 11 frames are dropped; in spectroscopic mode, the quality factor corresponds to the χ^2 value of the linear fit (for each pixel).
- The photometric mode, during photometric exposure, for which, in nominal operation, 16 read frames are grouped in 4 groups while in between groups, 4 frames are dropped; in this mode, the quality factor corresponds to a flag identifying pixels with χ^2 value above a threshold; this threshold can be tuned from the ground.

The NISP instrument has other operating modes with specific detector acquisition scheme for calibration purposes or for debugging of the instrument.

[§]The total duration of the detector exposure sequence, including DCU preparation and one reset frame before the start of charge integration.

[¶]The duration the detectors are collecting light.

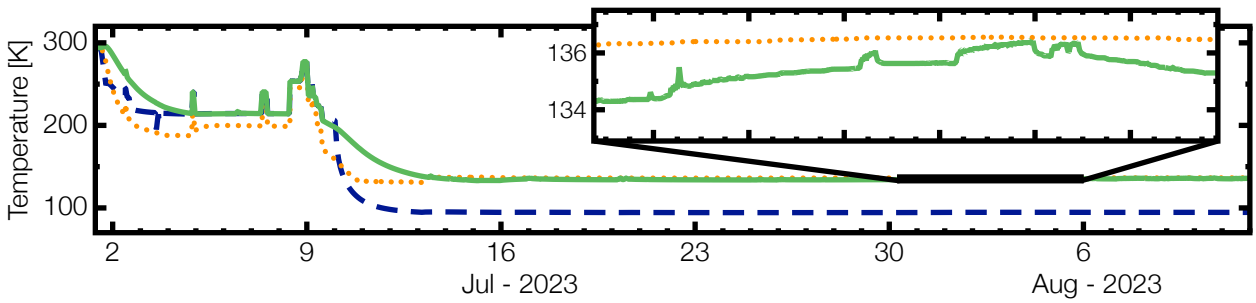

Figure 4: Variation of the temperature of the NISP optics (*solid line*), focal plane array (*dashed lines*) and detector SIDECARs (*dotted line*). The inset shows a detail of the variation of the optic temperature between the 31st of July to the 5th of August.

3. IN-FLIGHT STATUS

3.1 NISP temperatures

The ICU of the NISP instrument was powered on shortly after launch during the 'Launch and Early Orbit Phase' in order to monitor the cool-down of the instrument during the transit of the spacecraft to L2.

Figure 4 shows the cool-down by presenting the variation of the average[‖] temperature of the NISP optics (*solid line*), focal plane array (*dashed line*) and detector SIDECARs (*dotted line*) from launch till the end of the commissioning phase on the 12th of August 2023. Average temperature of the various subsystems stabilized to their operational temperature after the 14th of July 2023 with the NISP focal plane array at an average temperature of $\simeq$ 94.55 K, detector SIDECARs at about 136.40 K and optics at an average temperature of 134.73 K.

NISP's detectors, together with the DPU, were powered on the 12th of July after the focal plane cooled down below a temperature of 110 K. This threshold was defined to minimize the level of detector persistence, since ground tests demonstrated the dependency of the persistence signal to the detectors power-on temperature. At the time of detector power on (and at the operative temperature), detector baselines levels were tuned by setting the pixel reset voltages in order to set the dynamic range of the detector to their operational range [8].

The NISP instrument is designed for its optics to reach thermal equilibrium when the instrument is operating in the reference observation sequence of the survey, with regular activation of the NISP's wheels cryo-mechanism, which tends to warm-up the wheels, before the accumulated heat is dissipated. However, due to the various activities required to commission the spacecraft's subsystems and to calibrate the instruments, the cryo-mechanism of the wheels was irregularly activated with period for which NISP instrument was in standby, waiting for other activities to be completed. As consequence, during those activities the NISP's optics didn't reach a thermal equilibrium. These is illustrated within the inset of Figure 4 which shows fluctuation of the temperature of the wheels at the level of $\simeq$ 2 K peak-to-peak. Such thermal variation lasted all along performance verification phase and, once the survey started in February 2024, thermal variation of the optic lowered down to root-mean squared below 2 mK over a period of 3 days.

3.2 VIS-NISP co-focus

During NISP ground test campaign, the instrument focal length was measured to determine NISP's object plane. This was essential for precisely positioning the NISP instrument relative to the VIS, ensuring that when the telescope focalizes light onto the VIS (the primary instrument driving image quality), it also focalizes light onto the NISP's focal plane. Following the integration of the instrument onto the payload, cold tests were performed to verify the co-focus of the NISP instrument with the VIS. It's worth noting that the secondary mirror of the *Euclid* telescope is mounted onto a mechanism that allows three axis optical alignment. However, this set of verification were conducted under gravity, which deformed the primary mirror and consequently altered the

[‖] Averaged over the various probes sampling temperature of the subsystems.

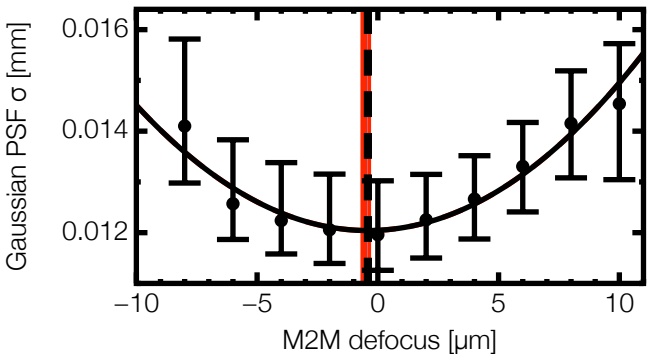

Figure 5: NISP image quality near the center of the FoV during secondary mirror fine focus alignment. Image quality is estimated from a Gaussian fit of the intensity profile of stars as function of level of defocus of the secondary mirror. Points with error bars show the median and the dispersion of the Gaussian width of the intensity profile measured across the population of identified stars. The continuous black line is a quadratic fits of the focus ramp. Vertical red line identify the VIS best focus position evaluated by Airbus Defence & Space (ADS) while the dashed black line indicates the NISP best focus position derived from the quadratic fit.

shape of the instrument's point spread function (PSF). It was therefore crucial to cross-check and validate the NISP and VIS co-focus in-flight.

For safety reason, the secondary mirror of the telescope was in park position during the launch. Before assessing optical performance of both instruments, Airbus Defence & Space performed the optical alignment by optimizing image quality on the VIS instrument. The procedure involved (i) a rough focus to evaluate the position of the secondary mirror providing the best focus, (ii) tilt/tip alignment of the secondary mirror at the estimated best focus position to end with (iii) a fine focus adjustment of the secondary mirror. During the alignment procedure, the VIS instrument image quality was used to evaluate image quality. However, the NISP instrument took images in $Y_{\rm E}$ band in parallel with the VIS during the rough and fine focus steps to control the co-focus between NISP and VIS.

The fine focus alignment procedure involved to acquire a focus ramp from $-10\,\mu$m to $+10\,\mu$m of defocus in steps of $2\,\mu$m. During fine focus adjustment, nominal exposure time was used to acquire both VIS and NISP images. Unsaturated stars were identified from the NISP exposure and their intensity profile were modeled with Gaussian function. The averaged width of the Gaussian was used as a proxy to estimate NISP image quality.

Figure 5 shows NISP image quality during fine focus alignment. NISP image quality improved, with smaller PSF size, as the defocus converges toward a value of $0\,\mu$m defocus, assumed to be the best focus position from the rough alignment. However, the best focus position isn't obtained at a $0\,\mu$m defocus. Instead, a quadratic fit of the image quality as function of the defocus, yields to a best image quality at defocus of $-0.41\,\mu$m while best focus position derived from VIS image quality was at $-0.5\,\mu$m. The procedure checked image quality at various position of the FoV. For each position, the best-focus position evaluated from NISP image quality was found to be compatible with best-focus position derived independently from analyses of VIS image quality. This procedure confirmed the co-focus of the NISP instrument relative to the VIS, ensuring excellent image quality of the NISP instrument once the telescope is aligned with the VIS.

3.3 Grism and filter wheel alignment

Both, the grism and filter wheels, have a home sensor to recover a reference position during flight operations.

To have an alternative procedure in case of malfunctioning, during ground test campaign, we have developed a wheel alignment based only on acquired images. This allows us to verify and validate the wheels positions in-flight before the calibration of the instrument and before the start of the survey.

The verification of the grism wheel alignment is straightforward, since the spectral dispersion direction aligns with the orientation of the grisms. Any misalignment of the grism wheel induces a rotation in the dispersion

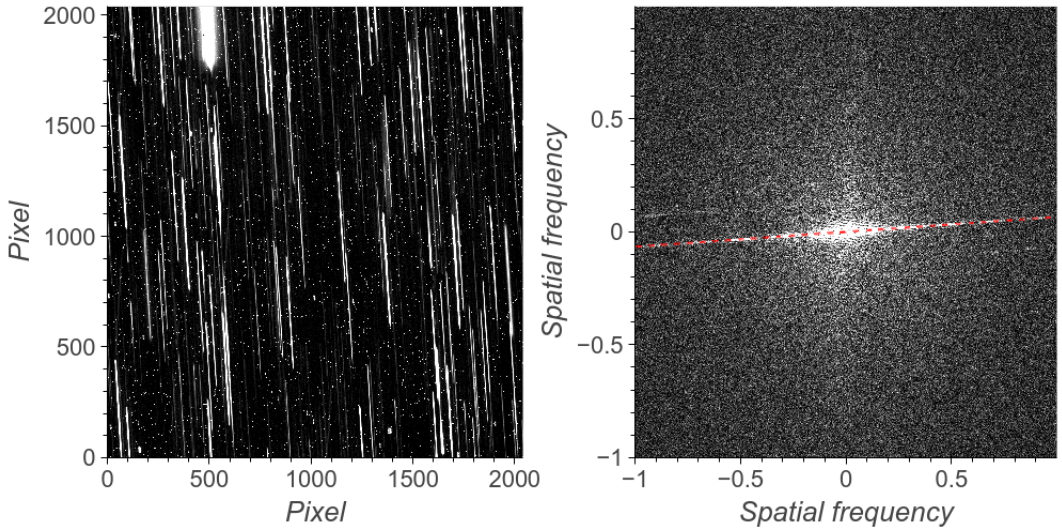

Figure 6: Evaluation of the grism wheel alignment from Fourier transform of spectroscopic exposure. On the left an exposure taken with one NISP's detector and the grism RGS180 at an angle of $-4°$ to its nominal position. On the right, the fast Fourier transform of the image on the left. The dashed line is a linear fit of the pixels with power larger than the 98.5 % quartil of the pixel population.

direction, which can be measured in Fourier space as illustrated in Figure 6. Due to the repetitive pattern induced by the spectra, slit-less spectroscopy's Fourier transform exhibits a power distribution in a privileged direction aligned with the dispersion direction. Measuring the angle in Fourier space provides an estimation of the wheel rotation angle. In Figure 6, we use linear fit of 'pixel' with power above 0.985 % of the power distribution to evaluate grism alignment angle.

Evaluating filter wheel misalignment is more complex than assessing grism alignment, because photometric exposures do not exhibit regular patterns as spectroscopic exposures do. However, when the filter wheel is misaligned, the nominal aperture of the filters is shifted away from the nominal beam center, producing vignetting that increases with the miss-alignment angle of the wheel. This is illustrated in Figure 7, that shows a raw image with a vignetting induced by a 12° offset of the filter $J_{\rm E}$. Despite small variation between detectors due to different detector response not corrected on those raw data, one can still distinguish a $\simeq 45°$ gradient in the dark background of the image which passes from light gray on the top left corner to dark gray in the bottom right corner. To emphasise this gradient, the image was resampled in 8×8 super-pixels by computing the mean value of pixels below 1060 ADU (Analog Digital Unit). Additionally, in Figure 7, any pixels with integrated signal above 1060 ADU were masked out.

To quickly evaluate the level of vignetting, we worked on NISP raw data. This allows us to obtain quick diagnostics of the filter wheel position, without waiting for the *Euclid* ground segment to access and process the data, that could take up to 24 hour depending of the queue of processes waiting to be run. For this analysis, we selected pixels with an integrated signal below 1060 ADU (i.e. $\simeq 6\,\gamma/{\rm s/px}$) to isolate the zodiacal light background. To increase statistics and better assess the vignetting, we summed the signal of the selected pixels along the $\rm Y_{MOSA}$ axis of the focal plane.

To verify the position of the filter wheel and validate filter wheel home position (i.e. the mechanical position set to be at 0°), we acquired for each filter a series of exposures with a wheel offset ranging either from $-8°$ to $+8°$ or from $-12°$ to $+12°$, both in steps of 4° which is the minimal step size of the cryo-mechanism. We computed for each exposure the sum along the $\rm Y_{MOSA}$ of the zodiacal background. Assuming that the wheel didn't involuntarily rotate since the last home position calibration, performed on the ground at warm temperature before the launch, the exposure of each filter taken with a wheel offset of 0° would have shown a minimal vignetting. Also, the profile of the vignetting should have been symmetric above and below offset of 0°. However, upon finding that this was not the case when we performed the check with offset ranging from $-8°$

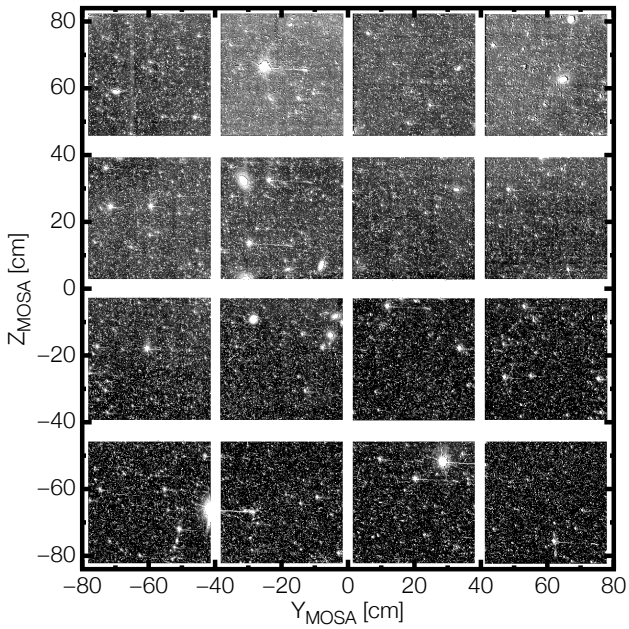

Figure 7: Single NISP exposure taken with the filter $J_{\rm E}$ at $-12°$ offset.

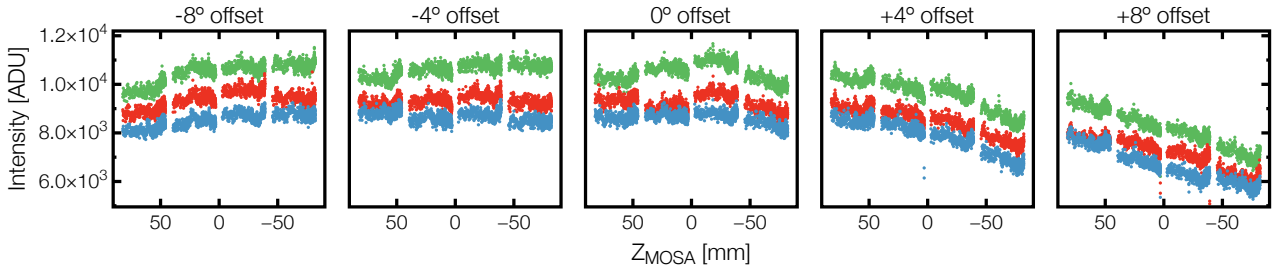

Figure 8.A **From left to right:** The wheel offset from the assumed correct alignment ranges from $-8°$ to $+8°$ in steps of $4°$. The asymmetry of the profile of the vignetting between offset $-8°$, $-4°$ and $+4°$, $+8°$ suggest that the home position has an offset of $+4°$.

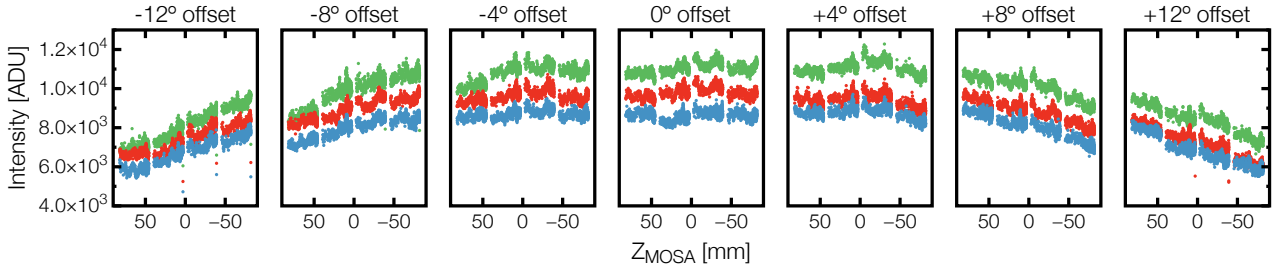

Figure 8.B **From left to right:** The wheel offset ranges from $-12°$ to $+12°$ in steps of $4°$. The symmetry of the profile below and above a $0°$ offset suggests that the home position is at the correct position.

Figure 8: Sum along $\rm Y_{MOSA}$ axis of the zodiacal background signal measured in-flight before (Figure 8.A) and after (Figure 8.B) re-calibration of the home position of the filter wheel and for filter $Y_{\rm E}$ (**blue**), $J_{\rm E}$ (**green**) and $H_{\rm E}$ (**red**). *To lighten the file, only 1 point out of 10 are displayed in the graphs.*

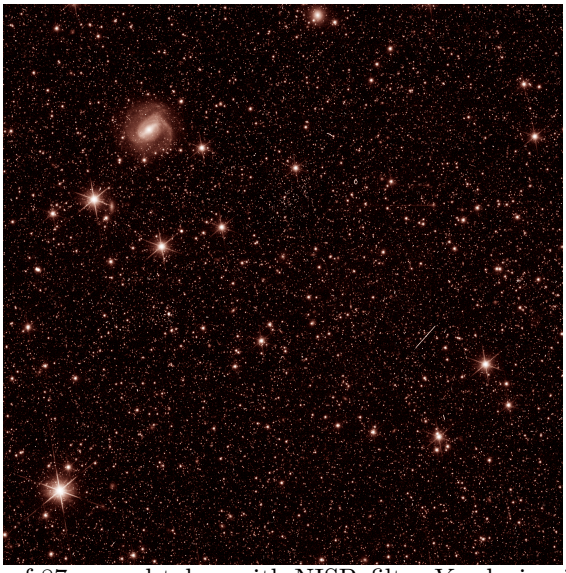

Figure 9: Single raw exposure of 87 second taken with NISP filter $Y_{\rm E}$, during instrument commissioning [9].

to +8° (see Figure 8.A), we re-calibrated the home position and repeated the procedure, this time with offset ranging −12° to +12° to increase the vignetting and better validate our new calibration (see Figure 8.B).

4. IN-FLIGHT PERFORMANCES

With more than 21 000 exposures taken with NISP during commissioning and performance verification phase (from July to December 2023) a preliminary assessments of the instrument performance was carried out. This performance is fully described in [3] and we report in this section a brief overview of in-flight image quality for the photometric and spectroscopic channel.

4.1 NISP in flight optical performance

Figure 9 reports a cut-out on a raw image taken during NISP commissioning in July 2023 shortly after the telescope focusing procedure carried out by Airbus Defence & Space was completed. The cut-out represents half the area of a NISP detector with a surface of $7' \times 7'$. This image did not undergo any processing with the exception of color scale adjustment and the application of a color palette, to emphasize details.

These raw data, taken with only 87 second of exposure, already demonstrates the high quality of the images. Cosmic-ray hits, featured as elongated track or single pixel with an excess signal, as well as detectors artefact, resulting in in-homogeneous pixel response, are visible on this raw image. All of these defects are removed or corrected during data reduction steps of the *Euclid* processing pipeline. Nonetheless and despite any cosmetic correction applied to the image, one can already appreciate the details of the spiral arm visible on the galaxy 2MASX J05571041−6750268 [10] located on the top left corner.

By design, the NISP's PSF is under-sampled, being almost at the diffraction limit and the pixel scale $\simeq 0\farcs3\,\mathrm{pixel}^{-1}$. The preliminary measurements of the PSF radii on stars, which include contribution NISP PSF broadened by telescope's PSF, telescope's jitters, and NISP detector effect as the inter-pixel capacitance (IPC), give a value ranging from $0\farcs21$ to $0\farcs27$ for the radii that contains 50 % of the total energy of the PSF (thereafter rEE50) and values ranging from $0\farcs37$ to $0\farcs55$ for the radii that contains 80 % of the total energy of the PSF (thereafter rEE80).

Based on the measurements of 1400 unsaturated stars across 76 different exposures, a model of the PSF has been created. This model revealS that the PSF exhibit small trefoil component extending from the *Euclid* primary mirror, resulting in a visible triangular shape for the PSF [3]. Despite this, our preliminary assessment of the image quality is consistent with a diffraction-limited NISP's PSF.

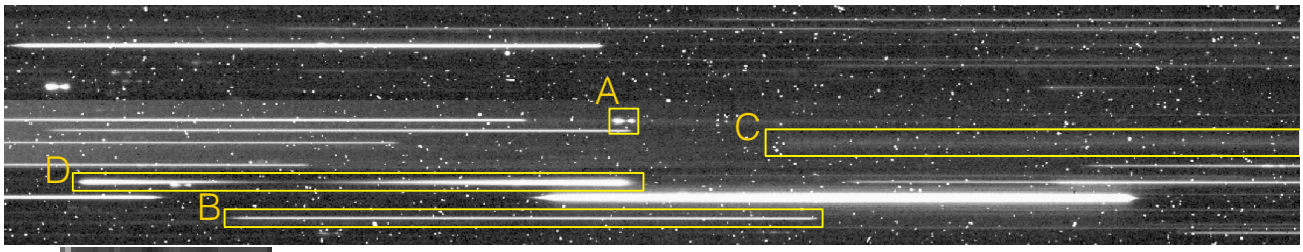

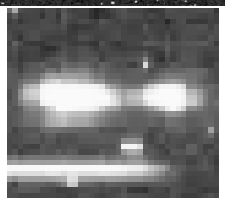

Figure 10.A Zoom-in on the 0^{th}-order component of a stellar spectra.

Figure 10.B Zoom-in on the 1^{st}-order component of a stellar spectra.

Figure 10.C Zoom-in on the 1^{st}-order component of a extended galaxy spectra.

Figure 10.D Zoom-in on the 2^{nd}-order component of a stellar spectra.

Figure 10: Cut-out on a raw spectroscopy exposure taken with grism RGS000 featuring several spectrograms. The majority of the small cluster (1 to 3 pixel of diameter) corresponds to cosmic rays hits. The highlighted regions A, B, C, and D correspond to the areas that are zoomed in on in the insets.

When considering image quality, ESA reported in [11] that at specific orientations of the spacecraft relative to the Sun, stray light originating from a small amount of reflected sunlight permeate the payload module cavity housing the two instruments. Due to the high sensitivity of the VIS instrument, this excess light significantly degrades the image quality when it impinges the VIS detectors. To date, the NISP instrument has not been affected by this excess stray light, most likely because the NISP is fully encapsulated within black multi-layer insulation. This insulation effectively reduces any light from undesired reflections. Additionally, the coating on the surfaces of the dichroic, filters and grisms is rejecting wavelength outside of the NISP bandpass, blocking visible sunlight to enter the NISP through the optical path.

4.2 NISP spectroscopy in-flight

Figure 10 shows a cut-out from a NISP spectroscopic exposure featuring several spectrograms. Due to the slitless nature of the NISP spectroscopic channel, all objects within the FoV produce spectrograms, which consist of a 0^{th}-order and 1^{st}-order. The different spectrograms present in the FoV may overlap each other and exposures with multiple dispersion direction are required to disantangle the different spectra from their contaminants. Thus the *Euclid* observations are observing the same field with four different dispersion orientation (see Figure 3).

Figure 10.A zooms-in on the 0^{th}-order component of a stellar spectrum. Because of the prism composing the grisms, 0^{th}-order components are slightly dispersed and extend over few tens of pixels. Their 'peanut' shape is a results of the blazing function of the grating engraved on the hypotenuse side of the prism, which forms the grism. The blazing function of the grating maximizes transmission of the 1^{st}-order at mid-bandpass (approximately 1500 nm for the red grisms). Consequently, the transmission of the 0^{th}-order has a minimum at the mid-bandpass (see [3]). Objects with significant continuum emission, such as stars, therefore exhibit this 'peanut' shape. Objects with strong emission lines and null continuum will have their 0^{th}-order of completely different shape and if a single emission line is located at mid-bandpass, the 0^{th}-order will not be visible at all.

The 1^{st}-order component of spectrograms are about 500 pixels long. Due to the point-like nature of stars, the 1^{st}-order component of stellar spectra (see Figure 10.B) is approximately 500 pixels long and thin. Again, due to the slit-less nature of the spectroscopic channel of the NISP instrument, 1^{st}-order component of the spectrograms of extended objects are folded with the object shape which spread out the signal in the cross-dispersion direction, as illustrated in the Figure 10.C which shows the the 1^{st}-order of an extended galaxy.

The NISP's grisms are designed to maximise transmission in the 1^{st}-order component. Transmission measurements conducted on the ground at the component level have shown that the transmission of the 1^{st}-order

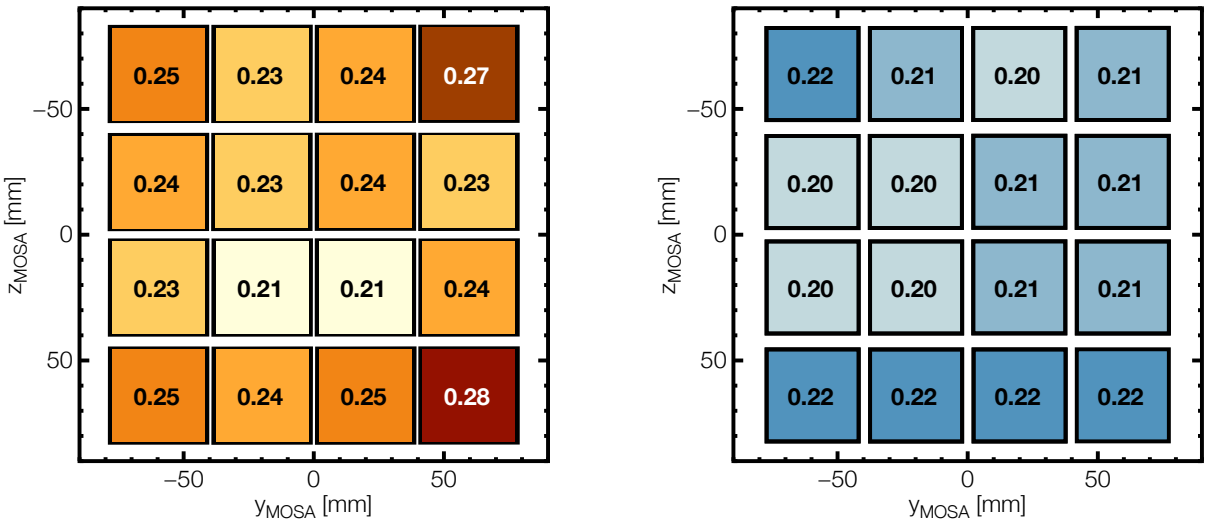

Figure 11: Preliminary estimation of the spectroscopic PSF rEE50 for the red grisms (left) and blue grism (right). Value of the rEE50 are averaged per detector and given in unit of arcsec.

component is approximately 84 %, while the 0^{th}-order transmission is below 2 % [12; 13]. The remaining fraction of the transmission is distributed in higher order components of the spectrograms with transmission below percent level. However, when objects are bright enough those higher order components will became visible. The most prominent is the 2^{nd}-order component that also exhibits a minimum at approximately mid-bandpass (see Figure 10.D). Spectrograms of bright stars in the FoV always exhibit the 2^{nd}-order component which may contaminate the 1^{st}-order of other objects.

An estimation of the spectroscopic PSF is obtained by measuring the width in cross-dispersion direction of the 1^{st}-order component of stellar spectrograms. These preliminary assessment yields to the values of spectroscopic rEE50 shown in Figure 11. As for the photometric ones, the spectroscopic PSFs are consistent with a diffraction-limited PSF, with an averaged rEE50 within scientific requirement of rEE50 $< 0\farcs3$, at wavelength above 1100 nm.

Figure 10 illustrates the grism dispersion on an image with the intensity depending on the pixel position rather than on the wavelength. To determine the corresponding wavelength at any pixel position, wavelength calibration was carried out during performance verification phase. This calibration involved the observation of planetary nebula SMC-SMP-20 [14], whose spectrogram observed with RGS000 is depicted in Figure 12. SMC-SMP-20 was selected for its compactness; with an apparent angular diameter of $0\farcs4$, the planetary nebula remains unresolved by the NISP, and appears as a point source. To obtain dispersion solution at any position of the NISP's FoV, the planetary nebulae was observed a total of 800 times. For each of the grisms (BGS000, RGS000, RGS000-4, RGS180 and RGS180+4) the pointing of the spacecraft was set such that the entire calibration sequence positioned the planetary nebula at five different positions per detector. For each of the positions, exposures were repeated to obtain a means to reduce the effect of cosmic-ray hits on the calibration.

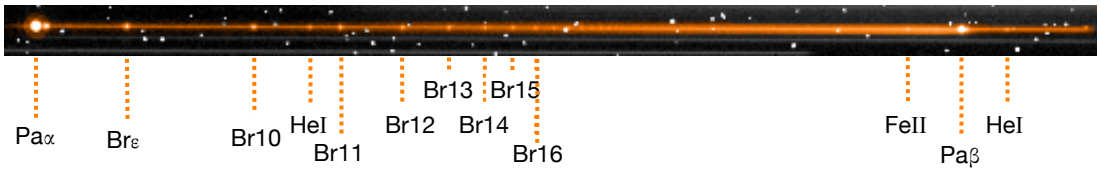

Figure 12: NISP 2D spectrogram of planetary nebula SMC-SMP-20. Known emission lines used to derive the dispersion law are labeled with their identified elements. The 2D spectrogram has been colourised for emphasis.

However, deriving calibration parameters for each of the grisms required several steps: The first step involves mapping the positions of the 0^{th}-order present in the FoV to the VIS astrometric solution; then the offset between the 0^{th}-order position to the 1^{st}-order position is evaluated using a reference wavelength in the 1^{st}-order. Next, the spatial curvature of the spectral trace is modeled using 2D Chebyshev polynomials. These initial three steps, achieved using stellar spectrograms, allow us to predict the pixel positions of the spectral trace for objects at any position in the FoV, but do not yet provide the corresponding wavelength. These is derived from the last step which consists in calibrating non-linear dispersion law using the distance relative to the reference wavelength of the emissions lines of the planetary nebula.

5. CONCLUSION

The NISP instrument onboard the *Euclid* spacecraft is operational since the 1st of July 2023, after the start of the 'Launch and Early Orbit Phase'. It reached the operational temperature in a couple of weeks, when NISP detector were powered on and commissioning and calibration activities started. Since then, the NISP operates nominally, showing excellent optical quality that exceeds its expected performance.

ACKNOWLEDGMENTS

The authors would like to acknowledge the late Favio Bortoletto and Olivier Lefevre for their exceptional contributions to the building and development of the NISP instrument. Their expertise and commitment left an indelible mark on this project.

The Euclid Consortium acknowledges the European Space Agency and a number of agencies and institutes that have supported the development of *Euclid*, in particular the Agenzia Spaziale Italiana, the Austrian Forschungsförderungsgesellschaft funded through BMK, the Belgian Science Policy, the Canadian Euclid Consortium, the Deutsches Zentrum für Luft- und Raumfahrt, the DTU Space and the Niels Bohr Institute in Denmark, the French Centre National d'Etudes Spatiales, the Fundação para a Ciência e a Tecnologia, the Hungarian Academy of Sciences, the Ministerio de Ciencia, Innovación y Universidades, the National Aeronautics and Space Administration, the National Astronomical Observatory of Japan, the Netherlandse Onderzoekschool Voor Astronomie, the Norwegian Space Agency, the Research Council of Finland, the Romanian Space Agency, the State Secretariat for Education, Research, and Innovation (SERI) at the Swiss Space Office (SSO), and the United Kingdom Space Agency. A complete and detailed list is available on the *Euclid* web site (`http://www.euclid-ec.org`).

References

[1] Euclid Collaboration, Mellier, Y., Abdurro'uf, and Acevedo Barroso, J. A., et al., "Euclid. I. Overview of the Euclid mission," *arXiv e-prints* , arXiv:2405.13491 (May 2024).

[2] Euclid Collaboration, Cropper, M., Al-Bahlawan, A., and Amiaux, J. et al, "Euclid. II. The VIS Instrument," *arXiv e-prints* , arXiv:2405.13492 (May 2024).

[3] Euclid Collaboration, Jahnke, K., Gillard, W., and Schirmer, M., et al., "Euclid. III. The NISP Instrument," *arXiv e-prints* , arXiv:2405.13493 (May 2024).

[4] Bougoin, M., Lavenac, J., and Pamplona, T., et al., "The SiC structure of the EUCLID NISP instrument," in [*Society of Photo-Optical Instrumentation Engineers (SPIE) Conference Series*], *Society of Photo-Optical Instrumentation Engineers (SPIE) Conference Series* **10562**, 105624J (Sept. 2017).

[5] Euclid Collaboration: Schirmer, M., Jahnke, K., and Seidel, G., et al., "Euclid preparation. XVIII. The NISP photometric system," *A&A* **662**, A92 (June 2022).

[6] Maciaszek, T., Ealet, A., and Jahnke, K., et al., "Euclid Near Infrared Spectrometer and Photometer instrument concept and first test results obtained for different breadboards models at the end of phase C," in [*Space Telescopes and Instrumentation 2016: Optical, Infrared, and Millimeter Wave*], MacEwen, H. A., Fazio, G. G., Lystrup, M., Batalha, N., Siegler, N., and Tong, E. C., eds., **9904**, 99040T, International Society for Optics and Photonics, SPIE (2016).

[7] Kubik, B., Barbier, R., and Chabanat, E., et al., "A New Signal Estimator from the NIR Detectors of the Euclid Mission," *PASP* **128**, 104504 (Oct. 2016).

[8] Cogato, F., Medinaceli Villegas, E., and Barbier, R., et al., "Euclid commissioning results: the Near Infrared Spectrometer and Photometer (NISP) signal detection chain," *Society of Photo-Optical Instrumentation Engineers (SPIE) Conference Series* , 13092–239 (June 2024).

[9] CREDIT: ESA/Euclid/Euclid Consortium/NASA, "Early commissioning test image – nisp instrument," (2023). https://www.esa.int/ESA_Multimedia/Images/2023/07/Early_commissioning_test_image_NISP_instrument2 – COPYRIGHT: CC BY-SA 3.0 IGO.

[10] Jones, D. H., Read, M. A., and Saunders, W., et al., "The 6dF Galaxy Survey: final redshift release (DR3) and southern large-scale structures," *MNRAS* **399**, 683–698 (Oct. 2009).

[11] ESA, "Stray light detected in euclid's vis instrument at particular angles," (2023). https://www.esa.int/ESA_Multimedia/Images/2023/09/Stray_light_detected_in_Euclid_s_VIS_instrument_at_particular_angles.

[12] Costille, A., Caillat, A., and Rossin, C., et al., "The EUCLID NISP grisms flight models performance," in [*Space Telescopes and Instrumentation 2018: Optical, Infrared, and Millimeter Wave*], Lystrup, M., MacEwen, H. A., Fazio, G. G., Batalha, N., Siegler, N., and Tong, E. C., eds., *Society of Photo-Optical Instrumentation Engineers (SPIE) Conference Series* **10698**, 106982B (July 2018).

[13] Costille, A., Caillat, A., and Rossin, C., et al., "Optical performance of NISP grisms flight models for EUCLID mission," in [*International Conference on Space Optics — ICSO 2018*], Sodnik, Z., Karafolas, N., and Cugny, B., eds., **11180**, 1118013, International Society for Optics and Photonics, SPIE (2019).

[14] Euclid Collaboration: Paterson, K., Schirmer, M., and Copin, Y., et al., "Euclid preparation. XXVII. A UV-NIR spectral atlas of compact planetary nebulae for wavelength calibration," *A&A* **674**, A172 (June 2023).